DOI: 10.1111/cgf.12913
Eurographics Conference on Visualization (EuroVis) 2016
K.-L. Ma, G. Santucci, and J. van Wijk
(Guest Editors)

Volume 35 (2016), Number 3

Source Inversion by Forward Integration in Inertial Flows

Tobias Günther and Holger Theisel

Visual Computing Group, University of Magdeburg

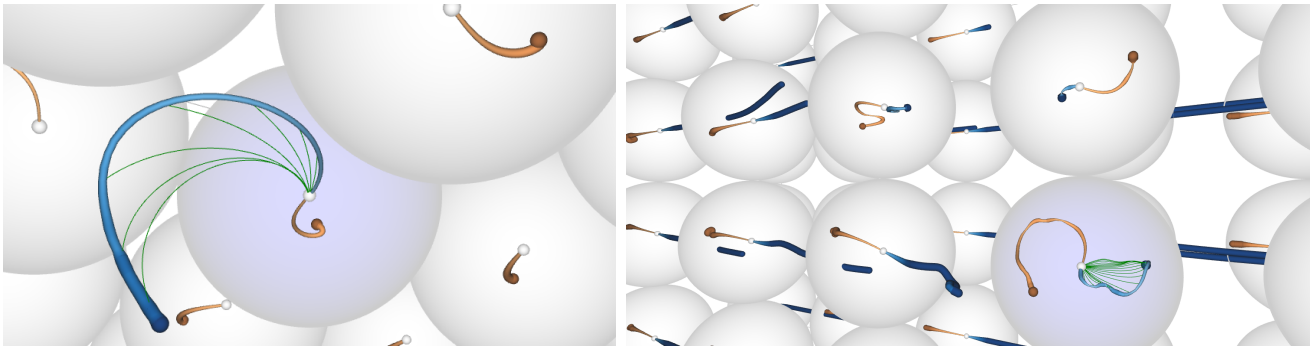

Figure 1: Visualization of the initial positions (blue curves) of inertial particle trajectories (green curves) that lead to the same location (small white sphere). At this location, a glyph is placed that depicts the velocities (orange curves), with which the inertial particles arrive. We solve the source inversion problem for left: TREFOIL and right: WALL-MOUNTED CYLINDER.

Abstract

Inertial particles are finite-sized objects traveling with a certain velocity that differs from the underlying carrying flow, i.e., they are mass-dependent and subject to inertia. Their backward integration is in practice infeasible, since a slight change in the initial velocity causes extreme changes in the recovered position. Thus, if an inertial particle is observed, it is difficult to recover where it came from. This is known as the source inversion problem, which has many practical applications in recovering the source of airborne or waterborne pollutions. Inertial trajectories live in a higher dimensional spatio-velocity space. In this paper, we show that this space is only sparsely populated. Assuming that inertial particles are released with a given initial velocity (e.g., from rest), particles may reach a certain location only with a limited set of possible velocities. In fact, with increasing integration duration and dependent on the particle response time, inertial particles converge to a terminal velocity. We show that the set of initial positions that lead to the same location form a curve. We extract these curves by devising a derived vector field in which they appear as tangent curves. Most importantly, the derived vector field only involves forward integrated flow map gradients, which are much more stable to compute than backward trajectories. After extraction, we interactively visualize the curves in the domain and display the reached velocities using glyphs. In addition, we encode the rate of change of the terminal velocity along the curves, which gives a notion for the convergence to the terminal velocity. With this, we present the first solution to the source inversion problem that considers actual inertial trajectories. We apply the method to steady and unsteady flows in both 2D and 3D domains.

Categories and Subject Descriptors (according to ACM CCS): I.3.3 [Computer Graphics]: Picture/Image Generation—Line and curve generation

1. Introduction

The study of inertial particles is an emerging field in flow visualization. Traditional flow visualization considers the trajectories of massless particles. However, many engineering problems require the observation of finite-sized objects immersed in the flow, so-called *inertial particles*. Examples are found in sand saltation modeling [SL99], soiling of cars [RSBE01], visual obscuration in helicopter landing maneuvers [KGRK14], formation of rain [Bor11], jellyfish feeding [PD09], plant spores and pathogens carried by atmospheric flow [BH02] and observations of charged particles in

magnetic fields [BZ89]. A particular application is the so-called *source inversion problem*, which arises in the source recovery of airborne or waterborne pollutions based on the observation of dispersed pollutants. While these are typically modeled along with diffusion processes as in Akçelik et al. [ABG*03], Boano et al. [BRR05], El Badia et al. [BHDH05] or Chow et al. [CKC08], the source inversion problem is non-trivial even when diffusion is neglected. With this simplification, a solution to the source inversion problem could only be approximated [HS08], and it was not possible to recover the initial velocity with which the pollutant entered the flow.

Since inertial particle motion is governed by an ODE, inertial trajectories can be computed as tangent curves of a higher dimensional vector field [GT14, GT15]. Yet still, source inversion is difficult, because backward integration is problematic in practice, even though it is theoretically well-defined [HS08, GT16]. Given an observation from which a backward integration is started, the recovered initial position and velocity of the inertial particle heavily depend on the observed velocity that we started with. In fact, a slight change leads to a completely different initial position, and most often the recovered initial velocity is extremely high and therefore implausible. Exploring different observed velocities until a plausible source is recovered is therefore a very tedious and impractical task. Instead of prescribing the observed position $\mathbf{x}$ and the observed velocity $\mathbf{v}$, the idea of our approach is to prescribe the observed position and an *initial velocity* $\mathbf{v}_0$: we assume that particles can start from any spatial location but with a fixed initial velocity $\mathbf{v}_0$. Such assumption is justified, for instance, when the pollutant is released from rest.

We formulate the following two problems to solve in this paper:

1. Given an observation point $\mathbf{x}$, from which points $\mathbf{c}$ in the spatial domain will an inertial particle integration with initial velocity $\mathbf{v}_0$ starting at t pass through $\mathbf{x}$ after finite integration time τ?
2. With which velocities $\mathbf{v}$ can such particle pass through $\mathbf{x}$?

We show that for both problems the solutions are one-parametric sets of points (Problem 1) or vectors (Problem 2). In fact, we show that all solutions of Problem 1 form a parametric curve $\mathbf{c}(\tau)$, which we call the *influence curve*. It is the collection of all points $\mathbf{c}$ in the spatial domain that have influence on $\mathbf{x}$ in the sense that inertial particles starting from $\mathbf{c}$ pass through $\mathbf{x}$. The main theoretical contribution of this paper is to show that *all* influence curves can be described as pathlines of *one* time-dependent vector field $\mathbf{h}(\mathbf{x},t)$, i.e., they can be extracted by a simple massless integration. Furthermore, the computation of $\mathbf{h}$ is based on forward integrated inertial particle trajectories only. Therefore, the computation is much more stable than a direct backward integration.

The solution of Problem 2 is also a one-parametric family of vectors $\mathbf{v}(\tau)$. This means that for a given observation point $\mathbf{x}$, inertial particles passing through it can have only "a few" possible velocities.

For the visualization, we systematically place observation points in the spatial domain and prescribe a user-defined initial velocity. After extraction, we interactively visualize the influence curves and display the velocities observed at the observation points using glyphs. As inertial particle trajectories converge to attracting manifolds in the spatio-velocity domain [MBZ06, HS08], we additionally encode the rate of change of the observed velocity along the influence curves, which gives a notion for the convergence to the terminal velocity in the attracting manifold. With this, we present the first solution to the source inversion problem that considers actual inertial trajectories. Our method provides the means to integrate inertial particles "backward", which enables a number of flow visualization and analysis methods that have previously been unaccessable for inertial particles. We demonstrate influence curves in a number of steady and unsteady flows in both 2D and 3D domains.

2. Background and Related Work

In this section, we briefly summarize the modeling of inertial particles and recent approaches to backward integration and source inversion. We end on a general summary of inertial particle research in visualization.

2.1. Modeling of Inertial Flow

Inertial particles are finite-sized objects that are carried by a fluid flow. In contrast to massless tracer particles, inertial particles have a certain density and diameter, and are thus subject to inertia. A number of forces act on them, including the force exerted by the flow itself, buoyancy, Stokes drag, the force exerted due to the mass of the fluid moving with the particle and the Basset-Boussinesq memory term, cf. Haller and Sapsis [HS08]. The Maxey-Riley equations [MR83] describe the full set of forces for spherical rigid particles. We refer to Farazmand and Haller [FH15] for a study of the properties of their solution and a summary of recent work on improvements of the model.

In many applications, several of the aforementioned forces are small enough to be neglected and thus, dependent on the application, several assumptions can be made. In the remainder of this paper, we follow the model described by Crowe et al. [CST98], i.e., we assume that particles are very small and that the density of the surrounding air is far smaller than the density of each particle. The model further neglects particle-particle interactions and assumes that the particles have no influence on the underlying flow, i.e., we assume one-way coupling. These assumptions are common in practice [SGL10, PSGC11, KGRK14, CGP*10, BBC*09, BBC*11] and lead to a simplified set of equations of motion.

Under these assumptions, Günther et al. [GT14, GT15] described the trajectories of inertial particles as tangent curves of a high-dimensional vector field, which models both the rate of change of particle position $\mathbf{x}$ and particle velocity $\mathbf{v}$. For an unsteady underlying flow $\mathbf{u}(\mathbf{x},t)$ in n-D with $n=\{2,3\}$, the autonomous governing m-D vector field, with $m=2n+1$, becomes:

$$\hat{\mathbf{p}} = \frac{\mathrm{d}}{\mathrm{d}t}\begin{pmatrix}\mathbf{x}\\ \mathbf{v}\\ t\end{pmatrix} = \begin{pmatrix}\mathbf{v}\\ \frac{\mathbf{u}(\mathbf{x},t)-\mathbf{v}}{r}+\mathbf{g}\\ 1\end{pmatrix} \quad \text{with} \quad \begin{pmatrix}\mathbf{x}\\ \mathbf{v}\\ t\end{pmatrix}(0) = \begin{pmatrix}\mathbf{x}_0\\ \mathbf{v}_0\\ t_0\end{pmatrix} \tag{1}$$

where $\mathbf{g}$ is a gravity vector (if not mentioned otherwise we set $\mathbf{g}=\mathbf{0}$), and $\mathbf{x}_0$, $\mathbf{v}_0$ and t_0 are the initial particle position, velocity and time. The response time r is characterized by particle diameter d_p and particle density ρ_p, as well as viscosity μ of the surrounding fluid:

$$r = \frac{d_p^2\,\rho_p}{18\,\mu} > 0 \tag{2}$$

Figuratively spoken, the response time is the time required for a

particle released from rest in a gravity-free environment to acquire 63% of the velocity of the carrying fluid, cf. [CST98]. Throughout the paper, we set as particle density ρ_p the density of dry sand, i.e., $\rho_p = 1600 kg/m^3$. The diameter d_p was set to $d_p = 300 \mu m$ if not mentioned otherwise. Note that these equations of motion hold for $d_p \ll \eta_k$, with η_k being the Kolmogorov length scale. The surrounding medium was assumed to be air, thus the viscosity was set to $\mu = 1.532 \cdot 10^{-5}\, kg/(m \cdot s)$. Given these parameters, r is in our experiments in the range $r \in [0.058, 0.928]$.

In [GKKT13], an inertial n-D flow map ϕ was introduced that maps a given initial condition (position, time, velocity) to the reached spatial location after integration. In this paper, we require flow map derivatives of the full inertial phase space, thus we consider the full m-D flow map of $\hat{\mathbf{p}}$ as

$$\hat{\phi}(\mathbf{x}, \mathbf{v}, t, \tau) = \begin{pmatrix} \phi(\mathbf{x}, \mathbf{v}, t, \tau) \\ \psi(\mathbf{x}, \mathbf{v}, t, \tau) \\ t + \tau \end{pmatrix} \tag{3}$$

where ϕ denotes the location and ψ the velocity of an inertial particle after integration duration τ when starting the integration at location $\mathbf{x}$ at time t with initial velocity $\mathbf{v}$. The gradient of $\hat{\phi}$ is a $m \times m$ matrix

$$\nabla\hat{\phi}(\mathbf{x}, \mathbf{v}, t, \tau) = \begin{pmatrix} \phi_{\mathbf{x}}(\mathbf{x}, \mathbf{v}, t, \tau) & \phi_{\mathbf{v}}(\mathbf{x}, \mathbf{v}, t, \tau) & \phi_t(\mathbf{x}, \mathbf{v}, t, \tau) \\ \psi_{\mathbf{x}}(\mathbf{x}, \mathbf{v}, t, \tau) & \psi_{\mathbf{v}}(\mathbf{x}, \mathbf{v}, t, \tau) & \psi_t(\mathbf{x}, \mathbf{v}, t, \tau) \\ \mathbf{0}_n^{\mathrm{T}} & \mathbf{0}_n^{\mathrm{T}} & 1 \end{pmatrix} \tag{4}$$

where $\phi_{\mathbf{x}}$, $\phi_{\mathbf{v}}$, $\psi_{\mathbf{x}}$, $\psi_{\mathbf{v}}$ are $n \times n$ matrices describing the partial derivatives of $\hat{\phi}$ with respect to $\mathbf{x}$, $\mathbf{v}$, and ϕ_t, ψ_t being the start time partials.

2.2. Backward Integration and Source Inversion

In vector field $\hat{\mathbf{p}}$, inertial particles can be integrated forward and backward in time. Backward integration, however, is problematic in practice. The recovered initial position and initial velocity are very sensitive to small changes of the observed velocity with which the backward integration was started. Fig. 2 illustrates the problem. Most often, the recovered initial velocity quickly becomes extremely high and therefore implausible. Closer observation of the topology of $\hat{\mathbf{p}}$ provides an explanation. As shown in [GT16], repelling critical points cannot exist in $\hat{\mathbf{p}}$. Thus during *backward* integration in the spatio-velocity phase space, an inertial particle is always subject to repelling behavior, as there are no attractors. Mograbi et al. [MBZ06] and Haller and Sapsis [HS08] explained that inertial particles converge during forward integration toward attracting manifolds in the spatio-velocity domain. Therefore, they are expected to repel away from them during backward integration [HS08].

The lack of a robust backward integration makes the *source inversion problem* challenging, which can be formulated as follows: Given an observed airborne or waterborne dispersed pollutant, compute the source of the pollution. Typically, the transport involves a diffusion process [ABG*03, BRR05, BHDH05, CKC08], though even without it, source inversion is non-trivial. For this simplified case, Haller and Sapsis [HS08] provide an approximate solution. Based on the observation that inertial particles are attracted toward manifolds in the spatio-velocity domain, they derived an ODE named *inertial equation*, which allows to move robustly *on* such an attracting manifold in both forward and backward direction. While

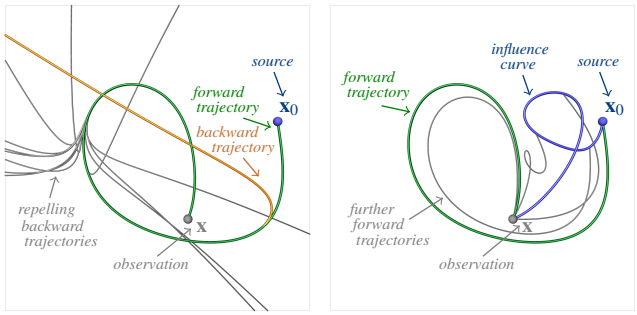

(a) Inertial backward integration exhibits strong repelling behavior. (b) Our *influence curves* avoid this problem.

Figure 2: Source inversion in left half of DOUBLE GYRE for $\tau = 9$ in (a): Starting from a source, forward integration takes an inertial particle to an observation. A backward integration, however, repels and does not reach the source (forward and backward curves are for numerical reasons not identical). Slight variations of the observation (in the order of 10^{-8}) lead to sooner repelling behavior. Backward integrated curves exhibit extreme velocities (particles exit the domain on rather straight tracks) and are therefore *implausible*. In (b), our *influence curve* connects all locations that lead during forward integration to the observation, which allows to recover the source.

this is a strong theoretical finding, there are three problems with this approach when applied to source inversion. First, the inertial equation lives in the spatial domain and thus it cannot recover the initial velocity with which the pollutant entered the flow. Second, for larger particles, instabilities occur [SH09] that drive inertial particles away from the attracting manifold on which the inertial equation is valid. For their particle model, Sapsis and Haller [SH09] derived a threshold that characterizes when this happens, which they applied in [SPH11]. Third, the inertial equation operates on the limit assumption that particles have reached the manifold. The method does not consider the accumulating inertia effects of actual inertial trajectories and it was shown by [GT16] that backward integration in the inertial equation cannot find topological structures such as separatrices of actual inertial trajectories.

In this paper, we solve the source inversion problem by considering actual inertial trajectories and we require forward integration only. For this, we describe possible sources as tangent curves of a derived vector field, yielding so-called influence curves. Modeling topological features or integral curves as tangent curves of possibly higher dimensional vector fields is a common approach in flow visualization. Streaklines [WT10] and timelines [WHT12] for instance have been modeled as tangent curves, same as the paths of critical points [TS03] or vortex corelines [WTGP11].

A problem related to source inversion is the computation of visitation maps. A visitation map determines for a given initial position the visitation frequency of all locations that may be reached in an uncertain flow. Bürger et al. [BFM*12] computed instant visitation maps by a Monte Carlo simulation that traces massive particle sets. Monte Carlo particle tracing could be applied to the source inversion problem as well by releasing particles from all locations in the domain and testing, which of them reach the observation point.

This, however, is very costly and does not provide a parametric description of the locations that reach the observation point.

2.3. Inertial Particles in Visualization

In the visualization community, Roettger et al. [RSBE01] simulated the soiling of cars and visualized particle concentration via heat maps. Based on the definition of an inertial flow map, Günther et al. [GKKT13] defined inertial integral curves and performed sand particle simulations around a helicopter in forward flight close to the ground. Günther and Theisel [GT14] extracted vortex corelines of inertial particles by applying techniques that were originally devised for traditional massless flow to the m-D vector field that governs the inertial motion. They formulated vortex extraction as an n-D parallel vectors problem. Later, they studied the finite-time separation behavior of differently-sized inertial particles [GT15]. They defined a separation measure, provided overview visualizations, visualized the separation in the space-time domain and used a coordinated plot to depict the temporal evolution of mass-induced particle separation. More recently, [GT16] conducted a full classification of the first-order critical points of the flow $\hat{\mathbf{p}}$ that governs inertial particle motion in the 2D steady case. Further, they devised an interactive glyph-based visualization that depicts the asymptotic behavior of inertial particles for varying initial positions and/or velocities.

3. Influence Curves

In the following, we define influence curves, describe a method to their efficient extraction and propose a visualization that depicts both the curves and the observable velocities.

3.1. Definition

We introduce the concept of the *influence curve* of an observation point $\mathbf{x}$ as a curve containing all points from which inertial integration with initial velocity $\mathbf{v}_0$ and start time t_0 ends in $\mathbf{x}$ after a certain integration duration τ. That is, we prescribe the *observed location* and the *initial velocity*. If not mentioned otherwise we set $\mathbf{v}_0 = \mathbf{0}$. We define all influence curves as a family of parametric curves $\mathbf{c}(\mathbf{x},\tau)$ so that

$$\phi(\mathbf{c}(\mathbf{x},\tau),\mathbf{v}_0,t_0,\tau) = \mathbf{x} \tag{5}$$

for all $\mathbf{x}$, curve parameterization τ and the family parameters $\mathbf{v}_0, t_0$. Given a curve $\mathbf{c}$, we can compute the observable velocity of particles arriving at $\mathbf{x}$ as $\psi(\mathbf{c}(\mathbf{x},\tau),\mathbf{v}_0,t_0,\tau)$ for any integration duration τ. Fig. 3 illustrates influence curves.

3.2. Extraction

The family of all influence curves can be characterized as pathlines of an n dimensional unsteady vector field $\mathbf{h}(\mathbf{x},t)$, starting at $t = t_0$:

$$\frac{d\,\mathbf{c}}{d\,\tau} = \mathbf{h}(\mathbf{c}(\mathbf{x},\tau), t_0+\tau). \tag{6}$$

Fortunately, vector field $\mathbf{h}$ has a simple form:

$$\mathbf{h}(\mathbf{x},t) = -\,{\phi_\mathbf{x}}^{-1}\left[\phi_\mathbf{v}\left(\frac{\mathbf{u}(\mathbf{x},t_0)-\mathbf{v}_0}{r}+\mathbf{g}\right)+\phi_t\right]-\mathbf{v}_0 \tag{7}$$

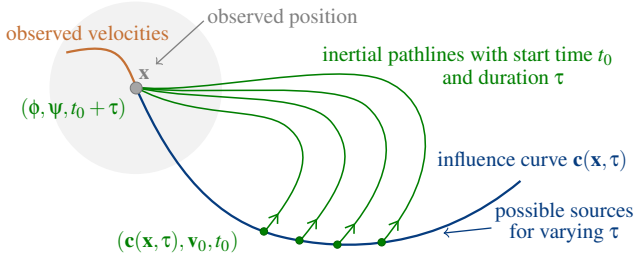

Figure 3: Given an observation $\mathbf{x}$, the influence curve (blue) is the union of all locations that lead an inertial pathline (green) to the observation $\mathbf{x}$. The velocity of arriving particles (orange) is shown in a glyph at $\mathbf{x}$. The glyph design is described later in Section 3.3.

where $\phi_\mathbf{x} = \phi_\mathbf{x}(\mathbf{x},\mathbf{v}_0,t_0,t-t_0)$, $\phi_\mathbf{v} = \phi_\mathbf{v}(\mathbf{x},\mathbf{v}_0,t_0,t-t_0)$ and $\phi_t = \phi_t(\mathbf{x},\mathbf{v}_0,t_0,t-t_0)$ are inertial flow map derivatives that can be computed by forward integration, cf. Eq. (4). Note that Eq. (7) is the main theoretical contribution of this paper. We refer to the appendix for a derivation of Eq. (7). With this, influence curves can be extracted via pathline integration in $\mathbf{h}$.

The definition of $\mathbf{h}$ raises another question: How far can we integrate forward in $\mathbf{h}$? Integration in $\mathbf{h}$ stops, when inertial flow maps or the influence curve itself leaves the domain or when the influence curve enters a critical point in $\mathbf{h}$. The latter is only expected for steady underlying flows $\mathbf{u}$. Consider a steady 2D center $\mathbf{u}(x,y) = (-y,x)^\mathrm{T}$ as shown in Fig. 4. While massless particles perfectly follow the circular motion, inertial particles spiral outward due to inertia. In fact, inertial particles that move for a longer period of time will be carried further outward. Consequently, influence curves must spiral inward, since all inertial particles released from the influence curve must reach the same observation point. Eventually, influence curves converge toward a critical point of $\mathbf{h}$. An example of this behavior in 3D is shown later in a steady flow in Fig. 12.

3.3. Visualization

For computing an influence curve via pathline integration in Eq. (7), we have to specify an *observation point* in the spatial domain from which the integration in $\mathbf{h}$ starts. In our visualizations, we systematically place the observation points and compute their corresponding

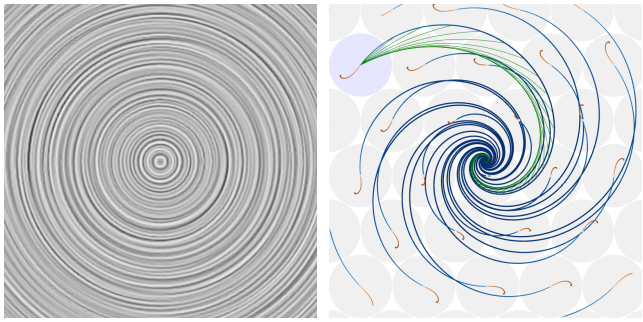

(a) LIC of $\mathbf{u}(x,y) = (-y,x)^\mathrm{T}$. (b) Influence curves in a center.

Figure 4: Inertial particles in a center flow, showing influence curves (blue), inertial pathlines (green, seeded from selected curve), as well as velocity glyphs (see Section 3.3).

influence curves. In 2D, the observation points are laid out in a hexagonal pattern in order to achieve the densest possible packing. In 3D, we decided to place them in a regular grid layout, as this makes the placement of axis-aligned clip planes easier.

We visualize the influence curves in the spatial domain (in blue) for a certain time range $[0, \tau]$, which is reported later in Table 1 for all figures. Additionally, we place a glyph at each observation point to depict the velocities with which the particles arrive (in orange). The glyphs have a circle shape in 2D and a sphere shape in 3D. They visualize the observed velocities in polar coordinates, with $\psi = \mathbf{0}$ being in the center and up to a certain user-specified upper velocity magnitude v_{max} at the boundary of the circle/sphere. The velocity of an arriving inertial particle is a point in the glyph and the union of velocities of all arriving particles forms a curve. The 2D case has similarities with the glyph designed in [GT16], though with the difference that our glyph encodes the observed velocity, whereas in [GT16] it depicts the initial velocity. In the 3D case, we cull the front faces of the spheres to allow looking inside them.

For both the influence curve in the spatial domain and the corresponding observed velocities in the glyph, we encode the change of the observed velocity with respect to the curve parameter. In particular, we map $1/(1+\partial\psi/\partial\tau)$ to line width and brightness. The change in the observed velocity gives a notion for the convergence of the particle velocity to the terminal velocity. The thicker and darker a curve segment the more likely has the observed velocity converged to the terminal velocity, since over time convergence gets slower. Note that this is only meant to give a notion for the convergence. Inertial particles may shortly be driven away from attracting (spatio-velocity) manifolds [SH09].

We allow the user to select a glyph by picking. For the selected glyph, we release a user-specified number of inertial pathlines (in green) from the selected influence curve. Then, all trajectories have in common that they reach the observation point. This pathline depiction is related to the eyelet particle tracing of Wiebel and Scheuermann [WS05], as they displayed pathlines that pass through a single point at different times for massless flows in order to capture the unsteady behavior of a time-dependent flow in a single steady image. In some cases, influence curves may clutter the view, especially in unsteady or in 3D flows. Thus, we allow the user to either show the influence curve of the selected glyph only (Fig. 8, left) or of all glyphs (Fig. 8, right).

4. Implementation

In the following, we share insights and observations we made about the numerical integration of the influence curves. Fig. 5 gives an example of the influence curve vector field in the DOUBLE GYRE, precomputed at $256 \times 128 \times 128$ in 100 minutes. In this flow, (massless) tracer particles stay inside the domain; inertial particles, however, do not. Due to inertia they might be dragged outside, depending on the particle response time, i.e., diameter, density and viscosity. This means, flow maps might leave the domain, and thus the influence curve field might not be defined at those places. Undefined areas are shown in Fig. 5 in black. Thus in these areas, influence curve integration stops and no further sources can be found. Also, influence curves themselves might leave the domain. We further elaborate on source inversion in bounded domains in Section 6.2.

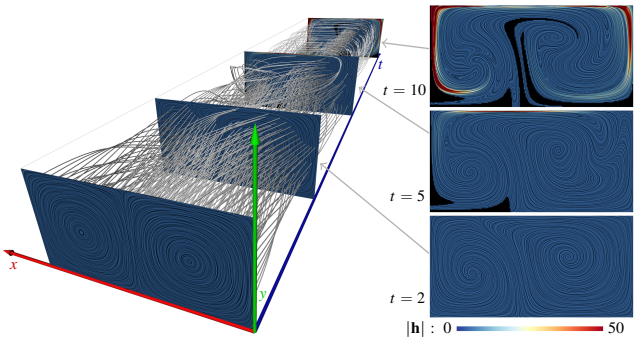

Figure 5: Influence curve vector field $\mathbf{h}(x, y, t)$ in the DOUBLE GYRE. Left: Space-time visualization of the influence curve vector field, containing several pathlines (i.e., influence curves). Right: Selected LIC slices, showing areas where $\mathbf{h}$ is undefined, since particles left the domain (black) and where the magnitude is high (red).

Another observation we made is that even though the DOUBLE GYRE flow has a rather moderate variation in the velocity magnitude, the influence curve field might have places with extremely high magnitude (variation of up to factor 3000). Fig. 5 (right) visualizes the magnitude by color-coding. In this example, high magnitudes occurred at later integration times ($\tau > 9$) close to the domain boundary, which causes numerical difficulties. We found that an adaptive integrator is mandatory in order to integrate through these areas. Thus, the influence curve integration in $\mathbf{h}$ is done using the adaptive Runge-Kutta-Fehlberg method (RK45).

If the domain should be densely covered with influence curves, the vector field $\mathbf{h}$ can be precomputed similar to [WT10]. If only few influence curves are shown, like in our glyph examples, a precomputation of $\mathbf{h}$ for all space-time locations does not pay off.

5. Results

We applied our method to a number of data sets. Note that some of them were studied in related CFD literature [HS08, SPH11]) and that the remaining examples mainly serve as synthetic testing ground for source inversion problems. In all flows, the spatial units are assumed to be in meters and time in seconds. The visualization parameters (v_{max}, t_0 and τ) are given for all figures later in Table 1.

5.1. Trefoil

Our first data set is courtesy of Candelaresi and Brandenburg [CB11] who simulated the decay of magnetic rings. In Fig. 6, we selected one particular 2D slice (steady, with velocity vectors projected into the 2D slice plane) and computed the influence curves for particles with different diameters. In this example, we make several observations that are in accordance with the expected behavior. First, we see that the smaller the particles are, the faster they align with the flow. This can be seen by the thickness and color of the lines, which represents the rate of change in the final velocity. Small particles converge to the terminal velocity faster, which is visible by the "drop shape" of the orange curves in the velocity domain, see Fig. 7. For small particles, the orange lines begin very thin and have a noticeable blob at the end, which represents the near-terminal velocity that almost all incoming inertial particles have reached. Further, we see that

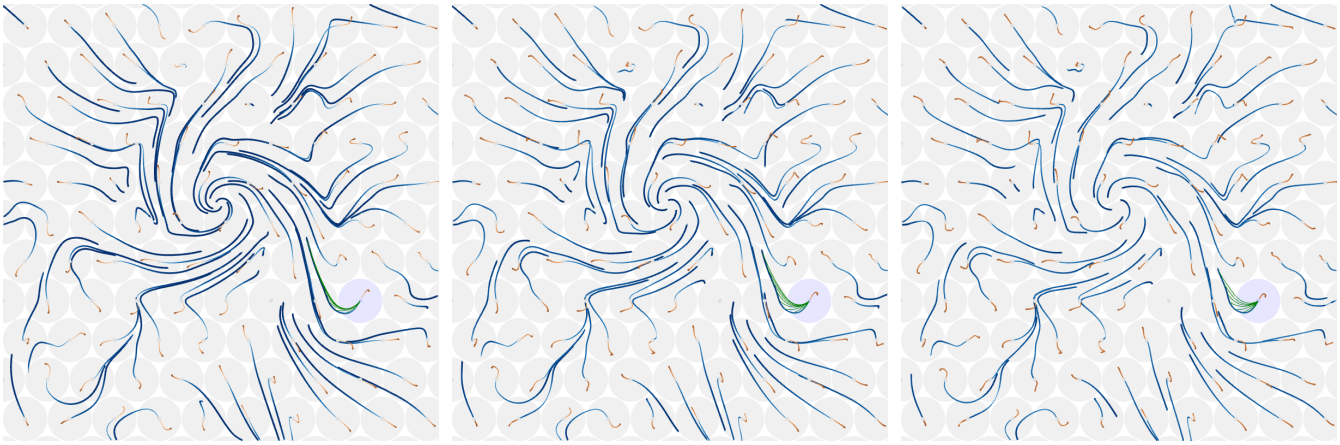

(a) $d_p = 200\,\mu m$ (b) $d_p = 300\,\mu m$ (c) $d_p = 400\,\mu m$

Figure 6: Visualization of all locations (blue curves) that reach the observation points (centers of gray circles). Here, we show the impact of particle size d_p in the TREFOIL 2D data set, together with inertial pathlines (green curves) for a selected glyph.

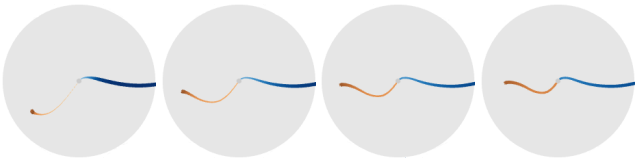

$d_p = 100\,\mu m$ $d_p = 200\,\mu m$ $d_p = 300\,\mu m$ $d_p = 400\,\mu m$

Figure 7: Typically, the observed velocities (orange) are distributed in a characteristic drop shape inside the glyphs. The orange line is parameterized by τ as well. The end of the line is thicker and represents the terminal velocity to which inertial particles converge.

inertia effects get stronger the larger the particles are, as inertial pathlines (green) deviate stronger from the influence curve (blue). This is expected, since larger particles have a higher response time, thus they take longer to respond to changes in the underlying flow.

In Fig. 8, we applied our method to the same data set in the original 3D domain. In the right image, patterns of coherent behavior emerge, which relate to the underlying magnetic ring structures. However, line depictions can get cluttered, thus we display in the left image only a selected influence curve. Fig. 1 (left) contains a detail view on one of the glyphs.

5.2. Forced-Damped Duffing

The FORCED-DAMPED DUFFING oscillator is a dynamical system that exhibits chaotic behavior. Its phase space has previously been used as a synthetic testing ground for observations of inertial particle dynamics in [HS11, GT15]. The phase space can be described and visualized as an unsteady 2D vector field of the form:

$$\mathbf{u}(x,y,t) = \begin{pmatrix} y \\ x - x^3 - 0.25y + 0.4\cos t \end{pmatrix} \tag{8}$$

here, in the spatial domain $D = [-2,2]^2$. Fig. 9 depicts influence curves for particles of different size and with varying gravity for the steady slice $t = 0$. It can be seen that influence curves of smaller particles are longer than those of bigger particles. This is due to the

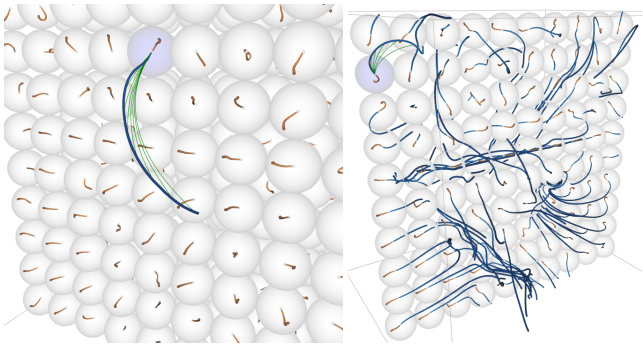

Figure 8: A dense sampling of a 3D domain, such as in the TREFOIL flow, might lead to cluttered influence curves. Left: only one influence curve is shown, right: all are shown.

smaller response time of small particles. All particles were released from rest and due to its larger response time, a large particle takes longer to accelerate and thus travels in the same time a shorter distance, compared to a smaller particle. Increasing gravity affects the course of inertial particles and thereby the influence curves.

5.3. Double Gyre

The DOUBLE GYRE [SLM05] is a well-known, periodic time-dependent 2D vector field. It is defined in the domain $D \times T = [0,2] \times [0,1] \times [0,10]$ as:

$$\mathbf{u}(x,y,t) = \begin{pmatrix} -0.1\pi \sin\left(f(x,t)\,\pi\right) \cos(y\pi) \\ 0.1\pi \cos\left(f(x,t)\,\pi\right) \sin(y\pi)\, \frac{\mathrm{d}}{\mathrm{d}x} f(x,t) \end{pmatrix} \tag{9}$$

with $f(x,t) = a(t)\,x^2 + b(t)\,x$, and $a(t) = 0.25\sin(t\,\pi/5)$ and $b(t) = 1 - 0.5\sin(t\,\pi/5)$. In Fig. 10, we extracted influence curves for different initial velocities. It can be seen that for $\mathbf{v}_0 \neq \mathbf{0}$, the orange line in the velocity glyph (depicting the observed velocities) does not start at the glyph center. The impact of the initial velocity on the particle trajectories can be seen by the green inertial pathlines.

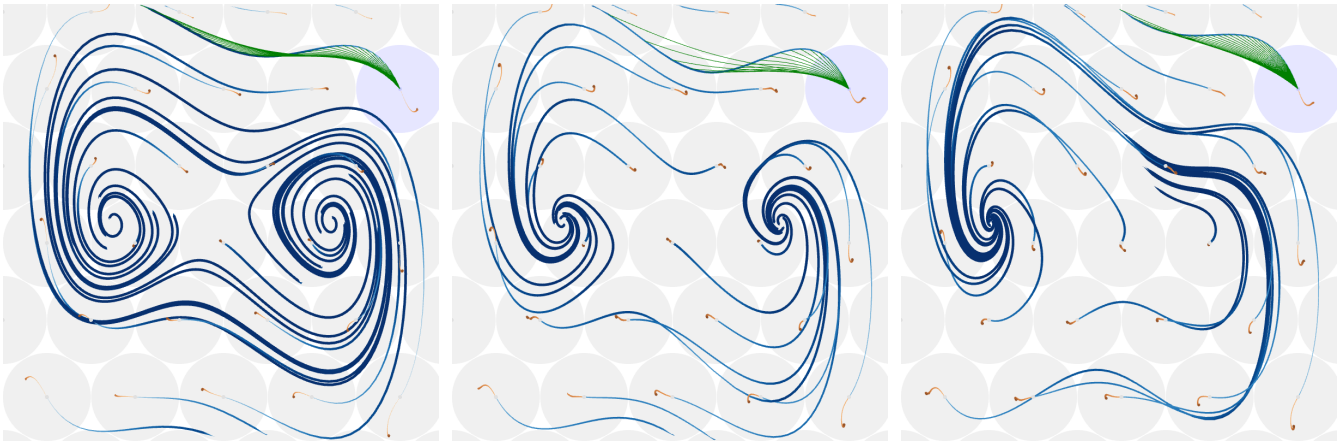

(a) $d_p = 200\,\mu m$, $\mathbf{g} = \mathbf{0}$ (b) $d_p = 400\,\mu m$, $\mathbf{g} = \mathbf{0}$ (c) $d_p = 400\,\mu m$, $\mathbf{g} = (0, -0.5)^T$

Figure 9: Influence curves in the phase space of the FORCED-DAMPED DUFFING oscillator for different particle sizes d_p and gravity $\mathbf{g}$. The larger the particles, the slower their response to changes in the underlying flow. Thus, they take longer to accelerate and as shown by the orange curves (observed velocity), they enter the observation points with less speed than the smaller particles. With increased gravity (downward), influence curves bend upward to accommodate the downward motion of inertial particles.

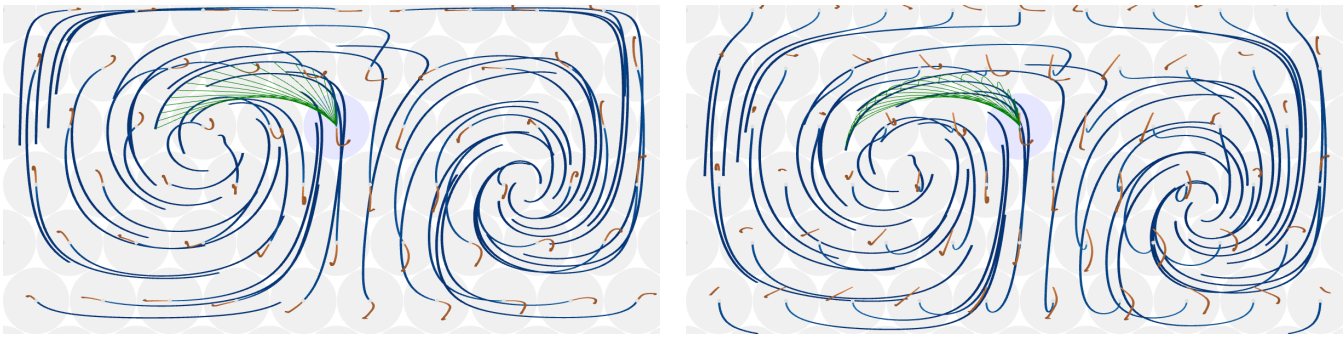

Figure 10: Influence curves for different initial velocities in the DOUBLE GYRE. Left: $\mathbf{v}_0 = (0,0)^T$, right: $\mathbf{v}_0 = (0,0.15)^T$. When inertial particles are not released from rest (right image), orange curves (observed velocities) no longer start at the glyph center.

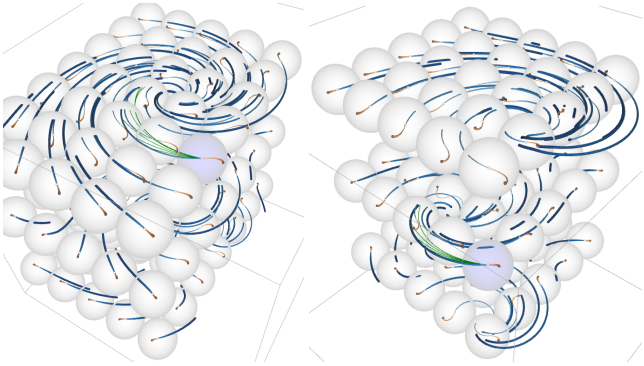

Figure 11: Influence curves in a steady TORNADO flow.

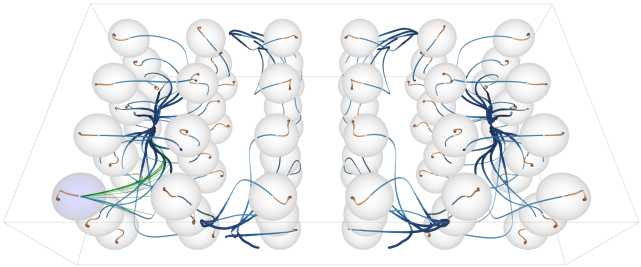

Figure 12: Influence curves in a symmetric RAYLEIGH-BÉNARD convection are separated into convection cells.

5.4. Tornado

Fig. 11 depicts a synthetic TORNADO data set from two different viewpoints. In 3D domains, glyphs occlude each other. Therefore, we allow the user to place clip planes in order to explore inner structures. In this example, we clipped away some of the glyphs to get a better view. The underlying flow has a relatively simple structure that is visible in the influence curves (blue) and their observed velocities (orange).

5.5. Rayleigh-Bénard

Fig. 12 shows a steady RAYLEIGH-BÉNARD convection, i.e., a thin layer of liquid that is heated from below. In this flow, separate convection cells are formed that rotate. Our visualization captures the symmetry of the domain and it can be seen that at least for the

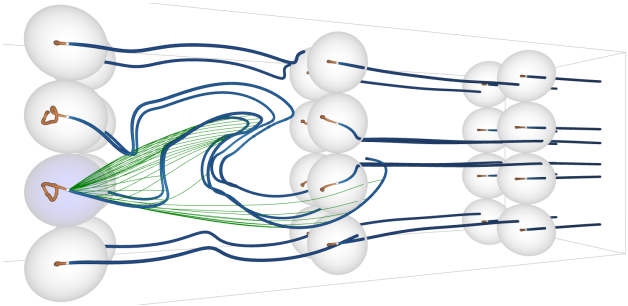

Figure 13: Influence curves (blue) in the unsteady wake of the 3D SQUARE CYLINDER sequence.

chosen observation points, influence curves are separated into the left and right halve of the domain. With ongoing influence curve integration, the curves reach critical points in $\mathbf{h}$, which are here inside the left-most and right-most convection cells.

5.6. Square Cylinder

The SQUARE CYLINDER flow [CSBI05] is a Navier-Stokes simulation of the 3D time-dependent flow around an obstacle. The uniformly resampled version of this vector field sequence was provided by Tino Weinkauf. Fig. 13 shows influence curves in the unsteady wake of the square cylinder. The two left-most glyphs in the middle show relatively strong variation in the observed velocity. The display of inertial pathlines (green) confirms the correctness of the extracted influence curves (blue).

5.7. Wall-mounted Cylinder

Frederich et al. [FWT08] simulated the time-dependent 3D air flow around a WALL-MOUNTED CYLINDER. In Fig. 14, influence curves are shown. This flow contains a laminar layer in the background and a turbulent layer in the foreground. In laminar areas, influence curves are rather straight, whereas especially in turbulent areas, the observed velocities vary strongly. Still, they form curves that can be extracted with our method. A close-up on the selected glyph in Fig. 14 is shown in Fig. 1 (right).

6. Discussion

In this section, we discuss the corresponding solution in the massless case, source inversion in bounded domains, an optional predictor-correct extension, the application of influence curves to another problem, and we provide performance measurements.

6.1. Relation to Massless Case

In the massless case, our influence curve is equivalent to a backward-integrated streakline. In the inertial case, a backward-integrated streakline also originates from a point $\mathbf{x}$, i.e., starting inertial pathlines from the streakline in forward direction will end up (spatially) at $\mathbf{x}$. We can, however, prescribe either of two things: the initial velocity (when starting from the streakline) or the observed velocity at $\mathbf{x}$ as in [GKKT13]. In this paper, we prescribe the initial velocity. The other is often problematic, as it requires inertial backward integration, which is difficult due to strong repelling behavior in the spatio-velocity domain [HS08, GT16], see Fig. 2a for an example.

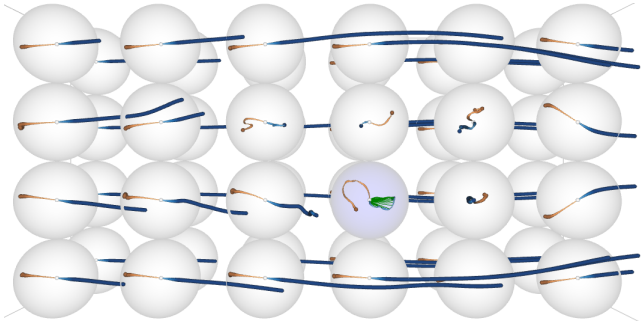

Figure 14: Unsteady flow around WALL-MOUNTED CYLINDER. Behind the obstacle, the flow is slow and turbulent.

6.2. Source Inversion in Bounded Domains

For the argumentation, we use the analogy to massless streaklines. Since streaklines represent individually advancing particle fronts, parts of a streakline might exit the flow domain, letting the streakline decay into disconnected pieces. If the streakline is integrated as a tangent curve (as in [WT10]), the integration terminates when the streakline leaves the domain and thus the disconnected pieces are not found. This means in our context that influence curves cannot recover further sources if the influence curve leaves the domain (even though it might reenter at a later time). In the future, we would like to investigate how points can be efficiently found at which an influence curve reenters the domain so that the integration can be continued. For the integration in $\mathbf{h}$, we can directly measure the integration error as $E(\mathbf{c}(\mathbf{x},\tau)) = \|\mathbf{x} - \phi(\mathbf{c}(\mathbf{x},\tau), \mathbf{v}_0, t_0, \tau)\|^2$, since an inertial pathline that was released from influence curve point $\mathbf{c}(\mathbf{x},\tau)$ should reach the observation point $\mathbf{x}$ exactly. Based on this, we would like to search the domain boundaries for reentry points.

6.3. Accumulating Errors

We described influence curves as tangent curves of a derived vector field. Generally, tracing curves this way is subject to accumulating numerical errors. With influence curves, however, this error can be measured (see Section 6.2), which allows for a predictor-corrector approach. After each integration step, the error can be reduced using Newton iterations. For the examples shown in the paper, the adaptive Runge-Kutta-Fehlberg (RK45) produced small enough errors. Nevertheless, they could be further reduced if the need arises.

6.4. Reachable Subspaces of the Spatio-Velocity Domain

In recent visualization papers on inertial particles [GKKT13, GT14, GT15, GT16], the full phase space of possible particle positions and velocities was considered. This becomes a mass-dependent and time-dependent 4D or 6D problem, which poses challenges on both the efficiency of the extraction methods and the visualization. Limiting the phase space allows to reduce the typically high dimensionality of computations. The need for such filter operations was identified in [GT14]. Assuming for instance that inertial particles are released from rest, we found in this paper that particles may reach a certain location only with a limited set of possible velocities. Further, we have shown that the set of initial positions that lead to the same location form a curve. By a dense sampling of the domain with

Data set	Glyphs	Time	v_{max}	t_0	τ
CENTER, Fig. 4	70	4.1	1	–	20
TREFOIL 2D, Fig. 6	180	3.1	1.2	–	2
TREFOIL 3D, Fig. 8	500	15.6	1.2	–	3
FORCED-D. DUFFING, Fig. 9	70	0.8	3.5	–	8
DOUBLE GYRE, Fig. 10	120	1.0	0.36	0	4
TORNADO, Fig. 11	147	5.4	5	–	3
RAYLEIGH-BÉNARD, Fig. 12	72	5.4	50	–	0.05
SQUARE CYLINDER, Fig. 13	8	14.9	2	10	14
WALL-M. CYLINDER, Fig. 14	72	69.9	11	0	10

Table 1: Numbers of glyphs, extraction time (in seconds) and parameters used in the figures, shown throughout the paper: maximal velocity shown in the glyphs v_{max}, start time t_0 (for unsteady flows) and integration duration τ, parameterizing the curve in $[0, \tau]$.

glyphs, we can visualize the spatio-velocity subspace that can actually be reached by inertial particles. Of course, this raises perceptual challenges, especially in 3D domains, when occlusion plays a role.

6.5. Performance and Parameters

We used an Intel Core i7-2600K CPU with 3.4 GHz. The number of glyphs, the extraction time of the influence curves (in seconds) and the respective parameters for v_{max} (maximal velocity shown in the velocity glyph), start time t_0 (if unsteady) and integration duration τ (parameterizing the curve in $[0, \tau]$) are listed for all data sets in Table 1. The extraction time is determined by the efficiency of the inertial pathline integration, which depends on the data set. In the analytic and simpler flows the influence curves were computed in a few seconds. In unsteady 3D flows, the extraction took up to 70 seconds. Generally, the further we integrate in $\mathbf{h}$, the more expensive the evaluation of an integration step becomes, since the pathlines involved in the flow map gradients have longer integration time τ. After extraction, the scene can be interactively explored and inertial pathlines can be interactively released from selected glyphs.

7. Conclusions

In this paper, we considered the source inversion problem of inertial dispersed particles. Given an observation point and a certain initial velocity, we recovered all locations that an inertial particle could originate from. We have shown that these locations form a curve, which we called *influence curve* and we extracted them by massless pathline integration in a derived time-dependent vector field. Thereby, all computations were based on inertial forward integration only. After extraction, we interactively displayed the influence curves in the spatial domain and placed glyphs at the observation points, illustrating the velocities with which the inertial particles arrived. With this, we presented the first solution to the source inversion problem that considers actual inertial trajectories rather than operating on attracting manifolds only [HS08]. This enables flow visualization methods that have previously been unaccessable for inertial particles. We believe that our work will spur further research in the extension of traditional massless flow visualization techniques (that are based on backward integration) to the inertial case.

Future work includes the search for filtering methods that allow to limit computations (such as inertial vortex detection) to regions in the spatio-velocity domain that are reachable by inertial flow. Dependent on the application, seeding regions and possibly varying initial velocities (modeled as probability distributions) play a role [GKKT13] that could be applied to further filter influence curves. Further, we would like to determine reentry points at which influence curves return back into the flow domain.

Acknowledgements

This work was supported by DFG grant no. TH 692/13-1.

Appendix

In the following, we derive Eq. (7). We search for the unknown vector field $\mathbf{h}$ that fulfills

$$\lim_{\Delta\tau\to 0} \frac{\hat{\phi}(\mathbf{x}+\Delta\tau\mathbf{h}, \mathbf{v}_0, t_0, \tau+\Delta\tau) - \hat{\phi}(\mathbf{x}, \mathbf{v}_0, t_0, \tau)}{\Delta\tau} = \begin{pmatrix}\mathbf{0}\\ \mathbf{v}_r\\ 0\end{pmatrix} . \quad (10)$$

Eq. (10) means that moving the starting point of the inertial particle integration from $\mathbf{x}$ to $\mathbf{x}+\Delta\tau\mathbf{h}$ and increasing the integration time from τ to $\tau+\Delta\tau$ should not change the location where the integration ends, while the change of the observed particle velocity is $\mathbf{v}_r$. In the following, we construct $\mathbf{x}+\Delta\tau\mathbf{h}$ at time $\tau+\Delta\tau$, i.e., the "next" location on the influence curve. For $\Delta\tau \to 0$ the flow map at $\tau+\Delta t$ is constructed by taking another "step" after the flow map at τ:

$$\begin{aligned}\hat{\phi}(\mathbf{x}+\Delta\tau\mathbf{h}, \mathbf{v}_0, t_0, \tau+\Delta\tau) = \hat{\phi}(\mathbf{x}+\Delta\tau\mathbf{h}, \mathbf{v}_0, t_0, \tau)\\ +\Delta\tau\,\hat{\mathbf{p}}(\hat{\phi}(\mathbf{x}, \mathbf{v}_0, t_0, \tau)) .\end{aligned} \quad (11)$$

The first summand of the right hand side contains the flow map at an infinitesimal close location in direction $\mathbf{h}$, which can be constructed from the flow map at $\mathbf{x}$ plus the flow map derivative in direction $\mathbf{h}$:

$$\begin{aligned}\hat{\phi}(\mathbf{x}+\Delta\tau\mathbf{h}, \mathbf{v}_0, t_0, \tau) = \hat{\phi}(\mathbf{x}, \mathbf{v}_0, t_0, \tau)\\ +\Delta\tau\,(\nabla\hat{\phi}(\mathbf{x}, \mathbf{v}_0, t_0, \tau))\begin{pmatrix}\mathbf{h}\\ \mathbf{0}\\ 0\end{pmatrix} .\end{aligned} \quad (12)$$

The second summand samples the phase space $\hat{\mathbf{p}}$ after flow map integration. This is the tangent of the curve at the reached location, which is also the flow map derivative in start direction $\hat{\mathbf{p}}$ at t_0:

$$\begin{aligned}\hat{\mathbf{p}}(\hat{\phi}(\mathbf{x}, \mathbf{v}_0, t_0, \tau)) &= (\nabla\hat{\phi}(\mathbf{x}, \mathbf{v}_0, t_0, \tau))\,\hat{\mathbf{p}}(\mathbf{x}, \mathbf{v}_0, t_0)\\ &= (\nabla\hat{\phi}(\mathbf{x}, \mathbf{v}_0, t_0, \tau))\begin{pmatrix}\mathbf{v}_0\\ \frac{\mathbf{u}(\mathbf{x},t_0)-\mathbf{v}_0}{r}+\mathbf{g}\\ 1\end{pmatrix}\end{aligned} \quad (13)$$

Inserting Eqs. (12) and (13) into Eq. (11), and inserting Eq. (11) in turn into Eq. (10) gives as condition for $\mathbf{h}$:

$$\lim_{\Delta\tau\to 0} \frac{\Delta\tau\,(\nabla\hat{\phi}(\mathbf{x}, \mathbf{v}_0, t_0, \tau))\left(\begin{pmatrix}\mathbf{h}\\ \mathbf{0}\\ 0\end{pmatrix}+\begin{pmatrix}\mathbf{v}_0\\ \frac{\mathbf{u}(\mathbf{x},t_0)-\mathbf{v}_0}{r}+\mathbf{g}\\ 1\end{pmatrix}\right)}{\Delta\tau} = \begin{pmatrix}\mathbf{0}\\ \mathbf{v}_r\\ 0\end{pmatrix} \quad (14)$$

Expanding the flow map gradient $\nabla\hat{\phi}$ using Eq. (4) and considering only the first n components of Eq. (14) (i.e., spatial subspace) gives

$$\phi_{\mathbf{x}}\,(\mathbf{h}+\mathbf{v}_0) + \phi_{\mathbf{v}}\left(\frac{\mathbf{u}(\mathbf{x}, t_0)-\mathbf{v}_0}{r}+\mathbf{g}\right)+\phi_t = \mathbf{0} , \quad (15)$$

which can be rearranged for $\mathbf{h}$ by inverting $\phi_{\mathbf{x}}$ to obtain Eq. (7).

References

[ABG*03] AKÇELIK V., BIROS G., GHATTAS O., LONG K. R., VAN BLOEMEN WAANDERS B.: A variational finite element method for source inversion for convective-diffusive transport. *Finite Elements in Analysis and Design 39*, 8 (2003), 683–705. 2, 3

[BBC*09] BENZI R., BIFERALE L., CALZAVARINI E., LOHSE D., TOSCHI F.: Velocity-gradient statistics along particle trajectories in turbulent flows: The refined similarity hypothesis in the Lagrangian frame. *Phys. Rev. E 80* (Dec 2009), 066318. 2

[BBC*11] BEC J., BIFERALE L., CENCINI M., LANOTTE A. S., TOSCHI F.: Spatial and velocity statistics of inertial particles in turbulent flows. *Journal of Physics: Conference Series 333*, 1 (2011), 012003. 2

[BFM*12] BÜRGER K., FRAEDRICH R., MERHOF D., , WESTERMANN R.: Instant visitation maps for interactive visualization of uncertain particle trajectories. In *Proc. SPIE 8294, Visualization and Data Analysis* (2012), SPIE, p. 82940P. 3

[BH02] BROWN J. K. M., HOVMØLLER M. S.: Aerial dispersal of pathogens on the global and continental scales and its impact on plant disease. *Science 297*, 5581 (2002), 537–541. 1

[BHDH05] BADIA A. E., HA-DUONG T., HAMDI A.: Identification of a point source in a linear advection-dispersion-reaction equation: Application to a pollution source problem. *Inverse Problems 21*, 3 (2005), 1121. 2, 3

[Bor11] BORDÁS R.: *Optical measurements in disperse two-phase flows: Application to rain formation in cumulus clouds*. PhD thesis, University of Magdeburg, 2011. 1

[BRR05] BOANO F., REVELLI R., RIDOLFI L.: Source identification in river pollution problems: A geostatistical approach. *Water Resources Research 41*, 7 (2005), WS07023. 2, 3

[BZ89] BÜCHNER J., ZELENYI L. M.: Regular and chaotic charged particle motion in magnetotaillike field reversals: 1. Basic theory of trapped motion. *Journal of Geophysical Research: Space Physics (1978–2012) 94*, A9 (1989), 11821–11842. 2

[CB11] CANDELARESI S., BRANDENBURG A.: Decay of helical and nonhelical magnetic knots. *Phys. Rev. E 84* (2011), 016406. 5

[CGP*10] CASCIOLA C. M., GUALTIERI P., PICANO F., SARDINA G., TROIANI G.: Dynamics of inertial particles in free jets. *Physica Scripta 2010*, T142 (2010), 014001. 2

[CKC08] CHOW F. K., KOSOVIC B., CHAN S.: Source inversion for contaminant plume dispersion in urban environments using building-resolving simulations. *Journal of Applied Meteorology and Climatology 47*, 6 (2008), 1553–1572. 2, 3

[CSBI05] CAMARRI S., SALVETTI M.-V., BUFFONI M., IOLLO A.: Simulation of the three-dimensional flow around a square cylinder between parallel walls at moderate Reynolds numbers. In *XVII Congresso di Meccanica Teorica ed Applicata* (2005). 8

[CST98] CROWE C., SOMMERFIELD M., TSUJI Y.: *Multiphase Flows with Droplets and Particles*. CRC Press, 1998. 2, 3

[FH15] FARAZMAND M., HALLER G.: The Maxey–Riley equation: Existence, uniqueness and regularity of solutions. *Nonlinear Analysis: Real World Applications 22* (2015), 98–106. 2

[FWT08] FREDERICH O., WASSEN E., THIELE F.: Prediction of the flow around a short wall-mounted cylinder using LES and DES. *Journal of Numerical Analysis, Industrial and Applied Mathematics (JNAIAM) 3*, 3-4 (2008), 231–247. 8

[GKKT13] GÜNTHER T., KUHN A., KUTZ B., THEISEL H.: Mass-dependent integral curves in unsteady vector fields. *Computer Graphics Forum (Proc. EuroVis) 32*, 3 (2013), 211–220. 3, 4, 8, 9

[GT14] GÜNTHER T., THEISEL H.: Vortex cores of inertial particles. *IEEE Trans. on Visualization and Computer Graphics (Proc. IEEE Scientific Visualization) 20*, 12 (2014), 2535–2544. 2, 4, 8

[GT15] GÜNTHER T., THEISEL H.: Finite-time mass separation for comparative visualizations of inertial particles. *Computer Graphics Forum (Proc. EuroVis) 34*, 3 (2015), 471–480. 2, 4, 6, 8

[GT16] GÜNTHER T., THEISEL H.: Inertial steady 2D vector field topology. *Computer Graphics Forum (Proc. Eurographics) 35*, 2 (2016), to appear. 2, 3, 4, 5, 8

[HS08] HALLER G., SAPSIS T.: Where do inertial particles go in fluid flows? *Physica D Nonlinear Phenomena 237* (May 2008), 573–583. 2, 3, 5, 8, 9

[HS11] HALLER G., SAPSIS T.: Lagrangian coherent structures and the smallest finite-time Lyapunov exponent. *Chaos 21*, 2 (2011), 023115. 6

[KGRK14] KUTZ B. M., GÜNTHER T., RUMPF A., KUHN A.: Numerical examination of a model rotor in brownout conditions. In *Proceedings of the American Helicopter Society* (May 2014), no. AHS2014-000343 in AHS 70th Annual Forum. 1, 2

[MBZ06] MOGRABI E., BAR-ZIV E.: On the asymptotic solution of the Maxey-Riley equation. *Physics of Fluids 18*, 5 (2006). 2, 3

[MR83] MAXEY M. R., RILEY J. J.: Equation of motion for a small rigid sphere in a nonuniform flow. *Physics of Fluids 26*, 4 (1983), 883–889. 2

[PD09] PENG J., DABIRI J. O.: Transport of inertial particles by Lagrangian coherent structures: Application to predator–prey interaction in jellyfish feeding. *Journal of Fluid Mechanics 623* (3 2009), 75–84. 1

[PSGC11] PICANO F., SARDINA G., GUALTIERI P., CASCIOLA C.: DNS of a free turbulent jet laden with small inertial particles. In *Direct and Large-Eddy Simulation VIII*, Kuerten H., Geurts B., Armenio V., Fröhlich J., (Eds.), vol. 15 of *ERCOFTAC Series*. Springer Netherlands, 2011, pp. 189–194. 2

[RSBE01] ROETTGER S., SCHULZ M., BARTELHEIMER W., ERTL T.: Automotive soiling simulation based on massive particle tracing. In *Data Visualization 2001*, Eurographics. Springer Vienna, 2001, pp. 309–317. 1, 4

[SGL10] SYAL M., GOVINDARAJAN B., LEISHMAN J. G.: Mesoscale sediment tracking methodology to analyze brownout cloud developments. In *Proceedings of the American Helicopter Society, 66th Annual Forum* (2010). 2

[SH09] SAPSIS T. P., HALLER G.: Inertial particle dynamics in a hurricane. *Journal of the Atmospheric Sciences* (2009). 3, 5

[SL99] SHAO Y., LI A.: Numerical modelling of saltation in the atmospheric surface layer. *Boundary-Layer Meteorology 91* (1999), 199–225. 1

[SLM05] SHADDEN S., LEKIEN F., MARSDEN J.: Definition and properties of Lagrangian coherent structures from finite-time Lyapunov exponents in two-dimensional aperiodic flows. *Physica D: Nonlinear Phenomena 212*, 3-4 (2005), 271–304. 6

[SPH11] SAPSIS T., PENG J., HALLER G.: Instabilities on prey dynamics in jellyfish feeding. *Bull Math Biol. 73*, 8 (2011), 1841–1856. 3, 5

[TS03] THEISEL H., SEIDEL H.-P.: Feature flow fields. In *Proc. Symposium on Data Visualisation* (2003), pp. 141–148. 3

[WHT12] WEINKAUF T., HEGE H.-C., THEISEL H.: Advected tangent curves: A general scheme for characteristic curves of flow fields. *Computer Graphics Forum (Proc. Eurographics) 31*, 2 (May 2012), 825–834. 3

[WS05] WIEBEL A., SCHEUERMANN G.: Eyelet particle tracing - steady visualization of unsteady flow. In *Proc. IEEE Visualization* (2005), pp. 607–614. 5

[WT10] WEINKAUF T., THEISEL H.: Streak lines as tangent curves of a derived vector field. *IEEE Transactions on Visualization and Computer Graphics (Proceedings Visualization 2010) 16*, 6 (November - December 2010), 1225–1234. 3, 5, 8

[WTGP11] WEINKAUF T., THEISEL H., GELDER A. V., PANG A.: Stable feature flow fields. *IEEE Transactions on Visualization and Computer Graphics 17*, 6 (2011), 770–780. 3